Chemical Engineering Journal 502 (2024) 157921

Contents lists available at ScienceDirect

Chemical Engineering Journal

journal homepage: www.elsevier.com/locate/cej

# Nitrous oxide abatement and valorization in an ammonia-fueled SOFC stack – Nitric oxide and electricity production

Celina Fernandes [a,b], Laura I.V. Holz [c,d], Francisco J.A. Loureiro [c,d], Miguel Duarte [a,b], Duncan P. Fagg [c,d,*], Adélio Mendes [a,b,*]

[a] LEPABE, Faculdade de Engenharia, Universidade do Porto, Rua Dr. Roberto Frias, 4200-465 Porto, Portugal
[b] ALiCE – Associated Laboratory in Chemical Engineering, Faculty of Engineering, University of Porto, Rua Dr. Roberto Frias, 4200-465 Porto, Portugal
[c] TEMA - Centre for Mechanical Technology and Automation, Department of Mechanical Engineering, University of Aveiro, 3810-193 Aveiro, Portugal
[d] LASI - Intelligent Systems Associate Laboratory, 4800-058 Guimarães, Portugal

ARTICLE INFO

*Keywords:*
Solid Oxide Fuel Cell stack
Nitrous oxide reduction
Ammonia oxidation
Nitric oxide
Electrochemical Impedance Spectroscopy
Distribution Function of Relaxation Times

ABSTRACT

Nitrous oxide ($N_2O$) is a harmful gas that strongly impacts climate change. Several strategies for denitrification have been addressed, where the use of solid oxide fuel cells (SOFCs) has been demonstrated to be attractive for $N_2O$ reduction and simultaneous electricity production. The reduction of $N_2O$ to $N_2$ is studied for the first time at the cathode of an SOFC, where ammonia is supplied to the anode as fuel. A diluted ammonia stream is particularly interesting since it is normally available in $HNO_3$ plants – the most important concentrated source of $N_2O$ emission – and is carbon-free. The combined reduction of $N_2O$ with the oxidation of $NH_3$ allows the production of nitric oxide (NO) at the anode, a valuable precursor for $HNO_3$ production.

This work uses a commercial SOFC stack comprehending six cells, equipped with membrane electrode assemblies of LSM-CGO || yttria-stabilized zirconia (YSZ) || YSZ-NiO. Electrochemical Impedance Spectroscopy (EIS) was successfully employed to characterize the stack performance. Data were analyzed by combining a Distribution Function of Relaxation Times (DFRT) and Equivalent Circuit Models (ECMs), for different operating conditions, namely in terms of temperature and fuel feed composition. Three major processes were identified at the anode: one related to the adsorption/desorption of reactants on the surface of the electrocatalyst, a diffusion process of charge carriers/intermediate species to the triple phase boundary (TPB), and a charge-transfer process at the TPB. The electrochemical production of nitric oxide (NO) was investigated, and a 20 % selectivity towards NO production and an energy stack efficiency of 88 % was obtained. Overall, the current work provides a critical first step toward using SOFC to perform efficient $N_2O$ electroreduction using diluted ammonia as fuel.

## 1. Introduction

One of the main goals of the European Union's climate change directives is to decrease greenhouse gas emissions by 42 % by 2030. Though nitrous oxide ($N_2O$) emissions are much smaller than $CO_2$, $N_2O$ is 300x more powerful greenhouse gas [1]; moreover, its concentration is steadily building up in the atmosphere, reaching 337 ppm in 2024 [2]. Besides, this compound is responsible for a variety of other environmental issues, including the depletion of the ozone layer. Anthropogenic emissions of $N_2O$ are mainly caused by the production of nitric acid ($HNO_3$), fertilizer production, and burning fossil fuels [1,3,4].

Nitric acid ($HNO_3$) is mostly produced by the *Ostwald* process [3,5] and the world production of nitric acid reached 150 million metric tons in 2023 [6]. It is synthesized based on the oxidation of $NH_3$ to nitric oxide (NO) over a platinum–rhodium catalyst alloy at 753 – 950°C [3] – a highly exothermic reaction:

$$4NH_3(g) + 5O_2(g) \rightarrow 4NO(g) + 6H_2O(g)\ \Delta H^0 = -95.2\,kJ\,mol^{-1} \quad (1)$$

*Acronyms:* BSE, Backscattered electrons; CGO, Cerium gadolinium oxide; DFRT, Distribution Function of Relaxation Times; ECM, Equivalent Circuit Model; EIS, Electrochemical Impedance Spectroscopy; HF, High-frequency; LF, Low-frequency; LSM, Lanthanum strontium manganite; MEA, Membrane electrode assembly; MF, Middle-frequency; SCR, Selective Catalytic Reduction; SEM-EDS, Scanning Electron Microscopy / Energy Dispersive Spectroscopy; SOFCs, Solid oxide fuel cells; TPB, Triple-phase-boundary; XRD, X-Ray Diffraction; YSZ, Yttria-Stabilized Zirconia.

* Corresponding authors.
*E-mail addresses:* duncan@ua.pt (D.P. Fagg), mendes@fe.up.pt (A. Mendes).

https://doi.org/10.1016/j.cej.2024.157921
Received 24 July 2024; Received in revised form 12 November 2024; Accepted 20 November 2024
Available online 22 November 2024

The produced nitrogen oxide is further oxidized to nitrogen dioxide and then to nitric acid:

$$2NO(g) + O_2(g) \rightarrow 2NO_2(g)\ \Delta H^0 = -114\,kJ\,mol^{-1} \quad (2)$$

$$2NO_2(g) + H_2O(g) \rightarrow 2HNO_3(g) + NO(g)\ \Delta H^0 = -117\,kJ\,mol^{-1} \quad (3)$$

Besides using platinum group metals catalysts, and depending on the temperature, the oxidation of ammonia yields different N-products with distinct oxidation degrees: $N_2$, $N_2O$, and NO [3]. Although the most thermodynamically favored reaction product is $N_2$, in the presence of the catalyst, a more complex situation occurs. At low temperatures (150 – 200°C), the only product is $N_2$; conversely, at higher temperatures, $N_2O$ starts to be formed [1,3], reaching its maximum at 402°C. The formation of NO, an intermediate product in the $HNO_3$ production, starts to be produced at 300°C, and its yield increases with the temperature. Under carefully controlled pressure and temperature, the NO selectivity is 95–97 %, while $N_2O$ selectivity is 1.5–2.5 %. Besides, the unreacted $NO_2$ is also a byproduct of the process and is released in the tail gas with NO and the formed $N_2O$ [7]. Despite the $N_2O$ being in higher concentration than NO and $NO_2$ (the $NO_x$), these two are also very detrimental and largely contribute to global warming [1]. Industrially, thermal or catalytic decomposition processes are used to abate $N_2O$ and $NO_x$, such as the selective catalytic reduction (SCR) process [1]. However, several drawbacks are associated with these processes, mainly the release of ammonia ($NH_3$) or carbon dioxide into the atmosphere, as these processes need a continuous feed of reducing agents, namely ammonia or methane [1]. Therefore, finding a cost-effective alternative to the SCR for denitrification coupled with the intensification of $HNO_3$ production would be a disruptive approach, due to the availability of $NH_3$ as a reducing agent.

SOFCs are electrochemical ceramic membrane reactors that have recently been considered for $N_2O$ abatement since they provide enhanced catalytic activity and selectivity, improved process integration, and easy reaction rate control [7,8]. Little literature reported this strategy applied to $N_2O$ decomposition, as reviewed by L. Alves *et al.* [1]. For example, Li *et al.* [9] assessed a tubular cell reactor incorporating yttria-stabilized zirconia (YSZ) electrolyte, a bore-side layer of Ni-YSZ composite anode, and a shell-side layer of LSM-YSZ composite cathode, where the anode was fed 30 mL $min^{-1}$ of hydrogen ($H_2$), as a fuel, while the cathode was fed with 50 mL $min^{-1}$ of either air or $N_2O$. When using air, a power density of 0.20 W $cm^{-2}$ was obtained at 750°C and a working potential of 1.15–1.17 V. At the same working potential, this power output was enhanced to 0.31 W $cm^{-2}$ when air was substituted with $N_2O$. Furthermore, the cathode showed significant activity for the decomposition of $N_2O$ (total conversion of ca. 60 %), uncovering an efficient methodology to reduce $N_2O$ emissions and produce electricity simultaneously.

Typically, SOFCs use $H_2$ as fuel, although this gas presents some drawbacks regarding storage and transportation [10]; following, it has been proposed to use ammonia ($NH_3$) instead of $H_2$ – it has a well-established distribution network and is largely available in chemical plants, especially in a plant that produces $HNO_3$. Besides, $NH_3$ presents physical and chemical properties that are particularly interesting; namely, $NH_3$ has high gravimetric and volumetric power density and a cost aligned with other synthetic fuels such as methanol [11]. The $NH_3$ oxidation at a SOFC is an endothermic reaction that allows a thermal energy integration with the cathode exothermal reaction with oxidant $N_2O$ [12,13]. Several researchers reported on this topic, highlighting its feasibility [12–17].

In the 80 s, Farr and Vayenas [18] reported the possibility of producing NO as a primary product from the $NH_3$ electrochemical oxidation using air as an oxidant and $NH_3$ as fuel in an SOFC. These authors used an yttria-stabilized zirconia tubular reactor, where platinum electrodes were deposited inside and outside the tube to allow the $NH_3$ oxidation at the anode and the $O_2$ reduction at the cathode. The pumped oxygen ions react with $NH_3$ at the anode side to produce NO and $H_2O$; $NH_3$ reacts catalytically with NO to produce $N_2$ and $H_2O$ – undesired side reaction. Increasing the residence time minimizes the undesired side reaction yield. The power density reported for the SOFC was 1 mW $cm^{-2}$. Decreasing the $NH_3$ flow rate originates a selectivity of 97 % at 24 % of conversion, displaying a power density of 7 μW $cm^{-2}$. Afterward, Sigal and Vayenas [18,19] reduced the anode side superficial active catalyst surface area, from 144 $cm^2$ to 2 $cm^2$, and they achieved a selectivity to NO of 97 % at 39 % conversion of $NH_3$, for a power density of 0.61 mW $cm^{-2}$.

This work proposes integrating the previously described strategies in a single device to increase the selectivity and power density. The new approach considers a SOFC fed with $NH_3$ – fuel – with the tail gas from a nitric acid plant containing $N_2O$. This approach responds to the urgent need to stop the emissions of $N_2O$, which results from the significant increase in the consumption of fertilizers [13] and, consequently, of $HNO_3$. The $N_2O$ at the cathode side is decomposed into nitrogen and oxygen, with subsequent oxygen reduction to $O^{2-}$, following the cathodic half-reaction:

$$N_2O(g) + 2e^- \rightarrow N_2(g) + O^{2-} \quad (4)$$

After, the $NH_3$ fed to the anode is oxidized to NO according to the anodic half-reaction

$$2NH_3(g) + 5O^{2-}(g) \rightarrow 2NO(g) + 3H_2O(g) + 10e^- \quad (5)$$

with high selectivity, closing the loop of the $HNO_3$ production – *cf.* equations (2) – (3). To the best knowledge of the authors, this arrangement is described here for the first time.

This project also aims to improve the phenomenological understanding of the $NH_3$ oxidation at the anode side, using two powerful characterization techniques: Electrochemical Impedance Spectroscopy (EIS) and the Distribution Function of the Relaxation Times (DFRT).

## 2. Materials and methods

### 2.1. Materials

The present study is based on experimental tests and results obtained on a lab solid oxide fuel cell stack, made of six planar cells, acquired from Almus AG company. Each cell is composed of a buffer layer made of $Ce_{0.8}Gd_{0.2}O_{2-\delta}$ (CGO20 – cerium gadolinium oxide), a thin $(ZrO_2)_{0.92}(Y_2O_3)_{0.08}$ (8YSZ) electrolyte, an active fuel electrode layer of NiO (nickel oxide)-8YSZ, and a cathode film of $(La_{0.75}Sr_{0.25})_{0.95}MnO_{3-\delta}$ (LSM – lanthanum strontium manganite) [20–23], as sketched in Fig. 1. The stack has an active area of 6 x 6 $cm^2$, containing 6 bipolar plates made of 1 mm Crofer 22 APU with etched flow fields, and alumina ($Al_2O_3$) tubes for the electric insulation of the metal conductors. The stack was equipped with a thermocouple placed in the center of the stack to record and control the temperature of the stack during the experiments. The oxygen concentration (or the oxygen partial pressure – $p_{O_2}$) was measured using a YSZ sensor (Kyocera) inserted at the outlet of the reactor.

The stack (Fig. 2) was tested on an in-house test bench and placed inside a furnace for temperature control. The setup was equipped with mass flow controllers (*Bronkhorst*) to regulate the flow rate of feed gases. The cathodic flow rate was fixed at 1680 mL $min^{-1}$ while the anode flow rate was varied between 300—–1200 mL $min^{-1}$. The experiments were conducted under different fuel compositions: ammonia ($NH_3$ – 99.9 % purity, *Air Liquide*) diluted in nitrogen ($N_2$ – purity 99.995 %, *Air Liquide*), with an ammonia concentration of 10 % and 20 %. In contrast, the cathodic atmosphere was, for all experiments, pure nitrous oxide ($N_2O$ – 99.9 %, Air Liquide). The temperature of the stack was fixed at 700°C for these experiments; at the end, and for a 20 % $NH_3$ fuel composition, the temperature was changed from 600°C to 800°C.

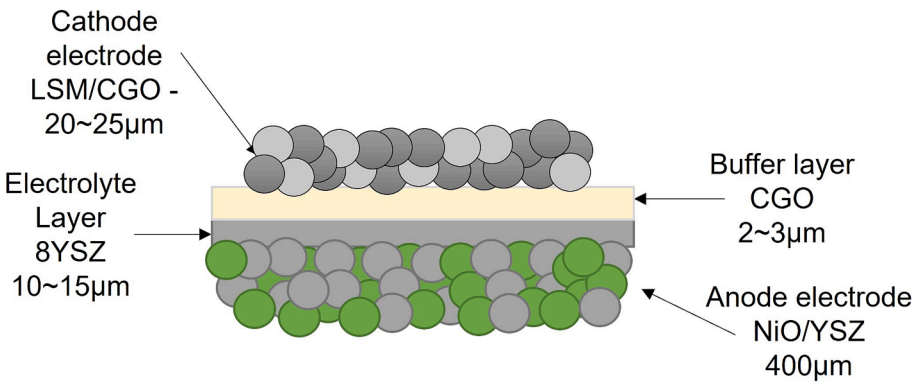


**Fig. 1.** Schematic representation of the commercial membrane electrode assembly (MEA).

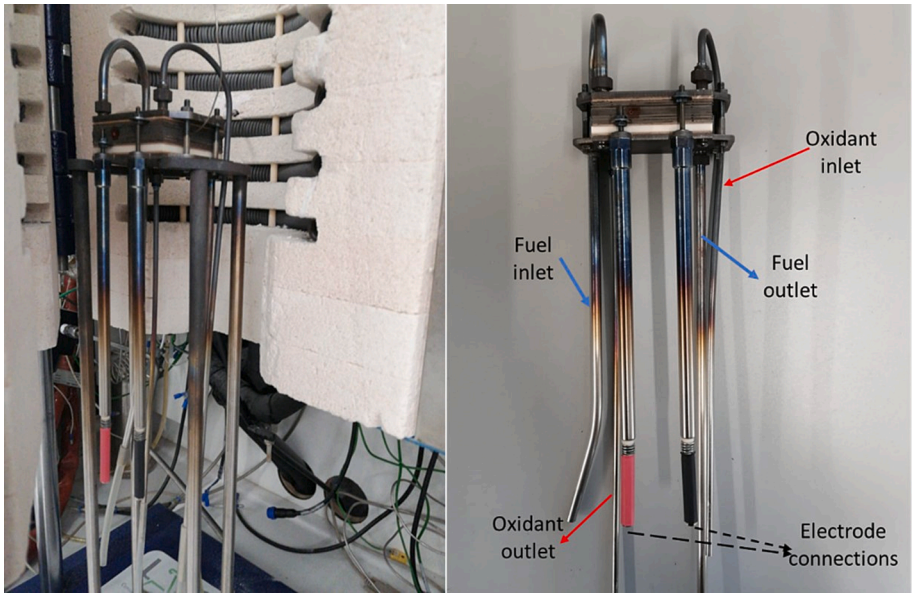


**Fig. 2.** Images of the SOFC stack in the present study.

### 2.2. Methods

The current–potential (*I-V*) characteristics of the stack were measured after the open circuit potential (OCP) became stable, using an *Autolab PGSTAT302N* potentiostat/galvanostat coupled with a 20 A Booster. The EIS measurements were performed using a 2-electrode configuration, with an applied signal amplitude of 20 mV, within a frequency range of 100 kHz to 0.01 Hz. The inlet gas composition and the furnace temperature were kept constant during the recording of the polarization curves. The polarization measurements were made for a period of 20 min under the chosen potential. A mass spectrometer (Pfeiffer, Quasdstar) was used to record the NO concentration at the anode gas outlet of the stack, while a gas chromatograph (Agilent 7890B) was used to analyze the cathode gas outlet.

The impedance spectroscopy results were analyzed using the software ZView. The EIS data were also analyzed by using the Distribution Function of Relaxation Times (DFRT) method. The DFRT spectrum, given by a function, $R_p \cdot G(\tau)$, was obtained by solving the Fredholm equation, which is represented by [24,25]:

$$Z(\omega_i) = R_{ohm} + R_p \int_0^{\infty} \frac{\gamma(\tau)}{1 + j\omega_i\tau} d\tau = R_{ohm} + R_p \int_{-\infty}^{\infty} \frac{G(\tau)}{1 + j\omega_i\tau} d\ln\tau \qquad (6)$$

with $G(\tau) = \tau \cdot \gamma(\tau)$ and $\int_{-\infty}^{\infty} G(\tau) d\ln\tau = 1$, where $\tau$ is the time constant, $\omega$ is the angular frequency, $R_{ohm}$ is the ohmic resistance, and $R_p$ is the total polarization resistance given by $R_p = R_T\text{-}R_{ohm}$, and $R_T$ represents the impedance at $\omega \rightarrow 0$. Fitting this equation to the experimental impedance – $Z_{exp}$ – to determine the distribution function $\gamma$ (ln $\tau$) is an intrinsically ill-posed problem [26]. Therefore, the distribution function of the relaxation times is calculated numerically. In this work, the DRTools software [27] was used to invert the EIS data from the frequency domain to the time domain, generating a DFRT spectrum. The DRTools implements the *Tikhonov* regularization procedure to obtain the distribution time function G($\tau$) [24,25]. The quality of the transformation was assessed by transforming the DFRT back to the EIS spectrum using the DFRTtoEIS software [28,29]. The DFRTtoEIS tool also allows fitting the DFRT peaks to automatically calculate the resistance, time constants, and capacitances for each response.

After the electrochemical experiments, the microstructure of a fractured cross-section of a membrane electrode assembly (MEA) was analyzed by Scanning Electron Microscopy (SEM), *Hitachi TM4000 plus*. The microscope was operated using an applied voltage of 15 kV, using a Backscattered Electron (BSE) detector. Energy dispersive X-ray analysis (EDS) was performed to provide the elemental mapping of the samples. X-ray diffraction (XRD) was performed to structurally characterize the materials of this work, using a *Rigaku SmartLab* diffractometer (Cu Kα radiation – 1.5406 Å, 40 kV, 30 mA). The patterns were obtained in the range of $10^\circ < 2\theta < 90^\circ$, scan speed of 3°C min $^{-1}$.

## 3. Results and discussion

### 3.1. General electrochemical characterization

The SOFC stack was characterized by electrochemical impedance spectroscopy (EIS) analysis under open circuit conditions, where the anode was fed with 1200 mL $min^{-1}$ of 20 % $NH_3$ balanced with $N_2$ and the cathode with 1680 mL $min^{-1}$ of 100 % $N_2O$ at the cathode; the stack was heated at 700°C. Nitrogen was chosen as a diluting gas since nitrogen is an inert gas that does not interfere with the reaction equilibrium of ammonia at high temperatures [30]; besides, nitrogen is cheap. The Nyquist plot, shown in Fig. 3a, displays an offset along the real $Z'$ axis at the highest frequencies, fitted to an inductive element (that results from the wiring and electrical connectors in the setup), followed by at least two relaxed semicircles. Fig. 3b) presents the distribution function of relaxation times (DFRT) representation, obtained from the Nyquist plot in Fig. 3a) using the *Tikhonov* regularization, where three peaks can be seen. The fitting parameters, time constant, τ, the resistance, R, and the capacitance, C (Table 1), were extracted from each peak. The validity of the DFRT was confirmed by reconstructing the original Nyquist plot and comparing it with the experimental values (Fig. 3a) [28,29]; the residuals plot, which was obtained from the two well-known relations [28,29]:

$$\Delta E_{\mathrm{real}}(\omega_i) = \frac{Z_{\mathrm{data,real}}(\omega_i) - Z_{\mathrm{fit,real}}(\omega_i)}{\left|Z_{\mathrm{data,real}}(\omega_i)\right|} \quad (7)$$

**Table 1**
Electrochemical parameters extracted from the *Tikhonov* regularization on the Nyquist plot obtained at 700 °C, for 20 vol% and 10 vol% of $NH_3$ at the anode, balanced with $N_2$, and 100 vol% of $N_2O$ at the cathode.

| DFRT peak | Parameter | 20 % $NH_3$ (700°C) | 10 % $NH_3$ (700°C) |
|---|---|---|---|
| $P_1$ | $\tau_{HF}$ / s | 2.77 x $10^{-3}$ | 4.58 x $10^{-4}$ |
| | $R_{HF}$ / Ω $cm^2$ | 22.52 | 127.01 |
| | $C_{HF}$ / F $cm^{-2}$ | 1.23 x $10^{-4}$ | 3.61 x $10^{-6}$ |
| $P_2$ | $\tau_{MF}$ / s | 1.45 x $10^{-2}$ | 1.77 x $10^{-2}$ |
| | $R_{MF}$ / Ω $cm^2$ | 31.01 | 773.88 |
| | $C_{MF}$ / F $cm^{-2}$ | 4.68 x $10^{-4}$ | 2.28 x $10^{-5}$ |
| $P_3$ | $\tau_{LF}$ / s | 2.95 x $10^{-1}$ | 3.71 x $10^{-1}$ |
| | $R_{LF}$ / Ω $cm^2$ | 63.19 | 700.80 |
| | $C_{LF}$ / F $cm^{-2}$ | 4.68 x $10^{-3}$ | 5.29 x $10^{-4}$ |

$$\Delta E_{\mathrm{imag}}(\omega_i) = \frac{Z_{\mathrm{data,imag}}(\omega_i) - Z_{\mathrm{fit,imag}}(\omega_i)}{\left|Z_{\mathrm{data,imag}}(\omega_i)\right|} \quad (8)$$

The obtained residuals plot – (Fig. 3c) – indicates a relative error of ± 0.15 % – Fig. 3c) – which should be considered rather good.

From Fig. 3b, it becomes clear that the response is dominated by the highest intensity peak ($P_3$) centered at $\tau_{LF}$ = 2.95 x $10^{-1}$ s, which is related to the low-frequency region of the EIS spectrum. Conversely, peaks centered at $\tau_{HF}$ = 2.77 x $10^{-3}$ s and $\tau_{MF}$ = 1.45 x $10^{-2}$ s – Fig. 3b) and Table 1 – should be related to the high- and the middle-frequency region of the EIS, respectively.

Due to the ammonia decomposition at the anode, the typical reaction

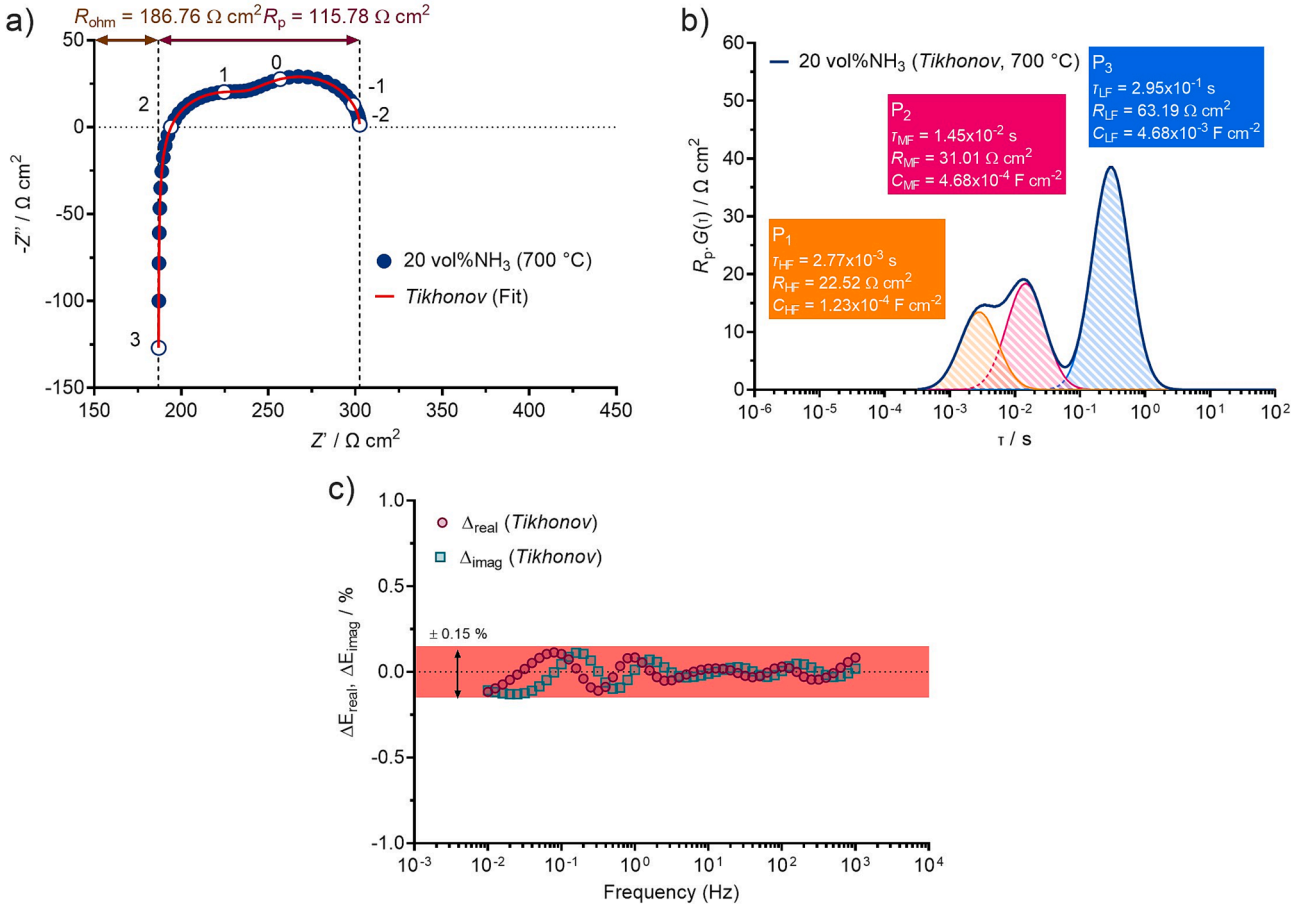


**Fig. 3.** a)Electrochemical impedance spectroscopy (EIS) spectrum obtained at 700 °C using an anode fuel mixture containing 20 % of $NH_3$ balanced with $N_2$, and a cathode oxidant gas containing 100 % of $N_2O$ – the numbers indicate the decades ($log_{10}$) of the measured frequency; b) the corresponding distribution function of relaxation times (DFRT) generated by the *Tikhonov* regularization; c) residuals plot between the experimental Nyquist plot and the fitted plot obtained from the *Tikhonov* regularization of the DFRT plot.

at the Ni-YSZ electrode is hydrogen oxidation [31–33]:

$$H_2(g) \rightarrow 2H_{ads} \quad (9)$$

$$H_{ads} \rightarrow H^+_{ads} + e^- \quad (10)$$

The $O_2$ is reduced at the cathode side:

$$O_2(g) \rightarrow O_{2(ads)} \quad (11)$$

$$O_{2(ads)} \rightarrow 2O_{(ads)} \quad (12)$$

$$2O_{(ads)} + 2e^- \rightarrow 2O^-_{(ads)} \quad (13)$$

where the following global cathodic reaction occurs [34,35],

$$O_2(g) + 2e^- + V_O^{\bullet\bullet} \rightarrow O_O^x \quad (14)$$

and this oxygen anion ($O^{2-}$ in $O_O^x$) is transported through the membrane electrolyte to react with the protons, at the anode side, forming water [31–33]:

$$2H^+_{(ads)} + O^{2-}_{(ads)} \rightarrow H_2O_{(ads)} \quad (15)$$

$$H_2O_{(ads)} \rightarrow H_2O\,(g) \quad (16)$$

The global anodic reaction can be described by [31–33],

$$H_2(g) + O_O^x(YSZ) \rightarrow H_2O\,(g) + V_O^{\bullet\bullet}(YSZ) + 2e^-(Ni) \quad (17)$$

where $O_O^x$ denotes an oxygen ion on the regular lattice site, $V_O^{\bullet\bullet}$ is a positively double-charged oxygen vacancy.

However, from the DFRT representation (Fig. 3b), a total of different 3 peaks were identified. In this regard, to be able to identify the origin of the associated processes, it was decided to study the SOFC stack under different conditions of fuel composition and temperature, addressed in the following sections.

### 3.2. *The effect of fuel composition on the electrochemical properties of the stack*

The SOFC stack was tested under 10 % of $NH_3$ balanced with $N_2$, fed to the anode side, resulting in a significant increase in both ohmic and polarization resistances (Table 1). This indicated that the anode needed to be further investigated. Since only the fuel composition of the anode was modified, under a fixed oxidant gas condition, *i.e.*, 100 vol% of $N_2O$, at fixed gas flow rates, the study will proceed with a focus on the anode reactions.

When the hydrogen partial pressure ($p_{H2}$) decreases, which is related to the concentration decrease of $NH_3$ from 20 % to 10 %, the hydrogen dissociative rate should also decrease, as well as the surface concentration of protons (higher polarization resistance); generally, the hydrogen dissociative adsorption/diffusion process at the anode occurs

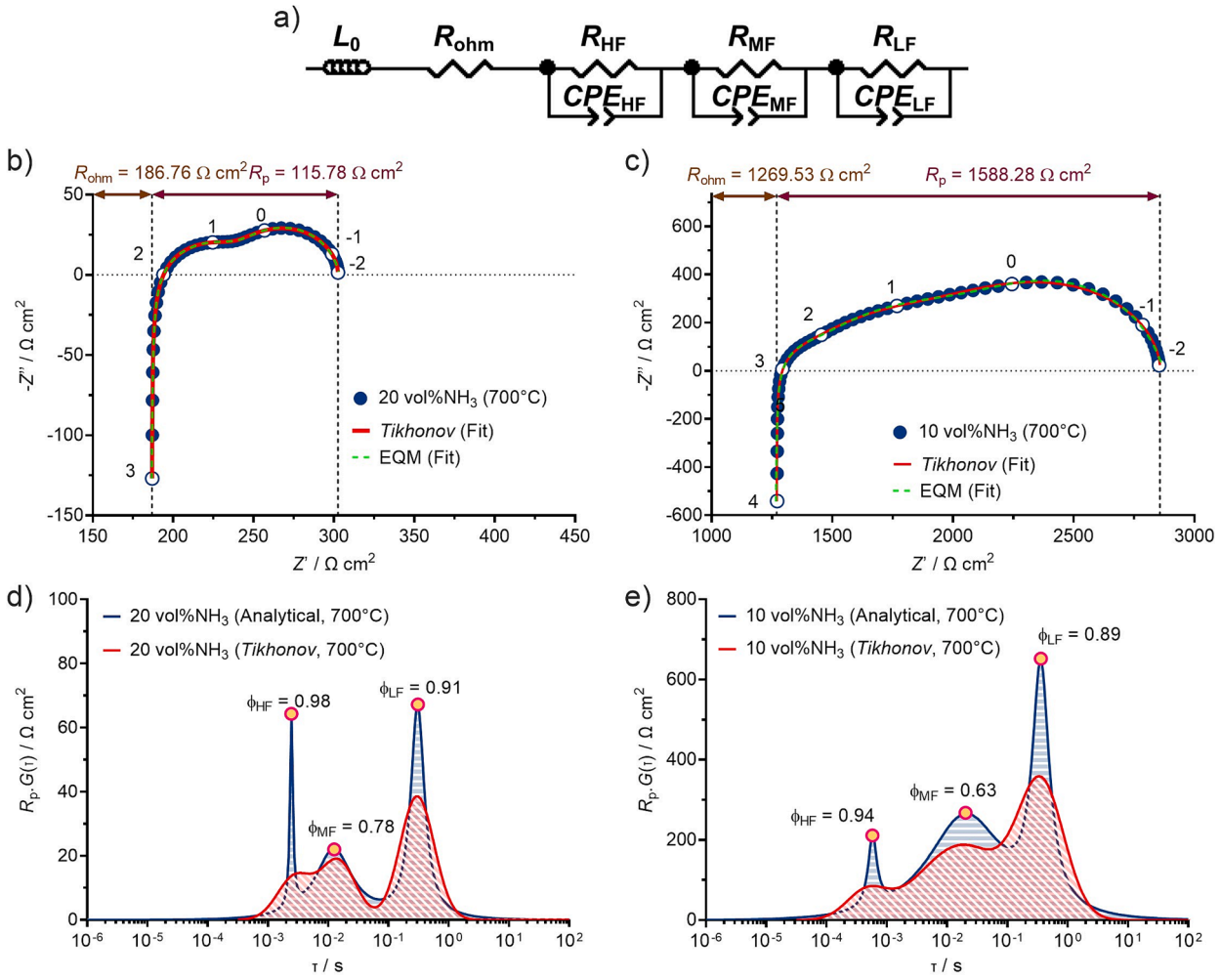


**Fig. 4.** Equivalent circuit model (ECM) used to fit the experimental Nyquist plot under open circuit voltage (OCV) conditions at a) 700 °C; corresponding EIS data obtained for b) 20 % of $NH_3$ balanced with $N_2$ and c) 10 % of $NH_3$ balanced with $N_2$, at the anode side; corresponding distribution function of relaxation times (DFRT) analyses generated by the *Tikhonov* regularization and the analytical procedure for d) 20 % of $NH_3$ and e) 10 % of $NH_3$, at the anode side.

in the low-frequency range [33,36], which should be here related to the $P_3$ peak in the DFRT plot (Fig. 3b). Nonetheless, it should be emphasized that all three peaks ($P_1$, $P_2$, and $P_3$) decrease when the $NH_3$ concentration decreases (Table 1), suggesting a more complex electrode transport mechanism.

Peak $P_1$ has a calculated capacitance in the range of $10^{-4}$F cm$^{-2}$ (Table 1), which is the typical range for the double-layer capacitance [36]. Therefore, $P_1$ should be related to the charge-transfer processes occurring at the triple phase boundaries (TPBs). The associated element in the SOFC of the middle-frequency peak, $P_2$, is more difficult to identify and deserves further attention.

The Nyquist plot was fitted to an equivalent electric circuit model (ECM), as sketched in Fig. 4a), using the software ZView 4.0. The parameters that characterize this circuit are an inductor ($L_0$) – fitted to the inductive tail –, the series resistance ($R_{ohm}$), a high-frequency electrode polarization process ($R_{HF}||CPE_{HF}$, assigned to peak $P_1$), a middle-frequency process ($R_{MF}||CPE_{MF}$, assigned to peak $P_2$) and low-frequency process ($R_{LF}||CPE_{LF}$, assigned to peak $P_3$). Here R||CPE elements are characterized by a resistance parallel to a constant phase element typically used to describe a semi-circle featured in the frequency domain. The CPE is used instead of a pure capacitor (C) due to the need to account for non-ideal behavior in real electrochemical systems and is used to represent a double-layer capacitance or other capacitance-related phenomena.

Fig. 4b) and c) show the experimental Nyquist plot, the model fitting, and the reconstructed Nyquist from the *Tikhonov* regularization; as for the *Tikhonov* regularization; also, the equivalent electric model shows a very good fitting. Fig. 4d) and e) compare the DFRT analysis with the *Tikhonov* and the electric circuit model. The DFRT of a $R||CPE$ circuit was obtained analytically and can be written as [24,25]:

$$R_i \cdot G(\tau)_{R||CPE} = \frac{R_i}{2\pi} \frac{\sin[(1-\phi)\pi]}{\cosh\left[\phi \ln\left(\frac{\tau}{\tau_0}\right)\right] - \cos[(1-\phi)\pi]} \tag{18}$$

with $\tau_0 = \omega_0^{-1} = \sqrt[\phi]{R_i \cdot Y_0}$, where $\omega$ corresponds to the angular frequency, $Y_0$ to the pseudo-capacitance, and $\phi$ to the exponent of the angular frequency from the $Z_{CPE}$ impedance.

The DFRT of the whole model is the sum of the three $R||CPE$ circuits [24,25]:

$$R_p \cdot G(\tau) = \sum_i R_i \cdot G(\tau) \tag{19}$$

with $R_p = \sum_i R_i$, where the area under the curve of $R \cdot G(\tau)$ equals $R_p$.

From Fig. 4d) and e), it can be observed that the number of individual peaks obtained by the *Tikhonov* regularization is the same as the one obtained from the DFRT of the equivalent model, thus confirming the presence of the three processes. Nonetheless, the DFRT analytical solution of the equivalent model provides sharp peaks, in which the full width of half maximum (*FWHM*) is directly related to the exponent of the angular frequency of the $Z_{CPE}$ impedance, $\phi$ (Eq. (17)). In contrast, the *Tikhonov* regularization was performed numerically using a Gaussian-type function, which, in present case, resulted in broader peaks. Nonetheless, when calculating the integral of the peaks, the obtained resistance values are very similar for both cases, as can be observed in Table 2.

**Table 2**
Values of resistance obtained by the analytic method and Tikhonov regularization.

| | Resistance | $R_{analytic}$ (Ω cm$^2$) | $R_{Tikhonov}$ (Ω cm$^2$) |
|---|---|---|---|
| 20 % $NH_3$ | $R_{HF}$ | 11.75 | 22.52 |
| | $R_{MF}$ | 45.62 | 31.01 |
| | $R_{LF}$ | 59.68 | 63.19 |
| 10 % $NH_3$ | $R_{HF}$ | 103.98 | 127.01 |
| | $R_{MF}$ | 871.38 | 773.88 |
| | $R_{LF}$ | 637.78 | 700.80 |

While $\phi_{HF}$ and $\phi_{LF}$ are in the range of 0.89 to 0.98, denoting values close to ideal capacitors ($\phi = 1$ for a pure capacitor, more uniform interface [37]), a much lower value can be observed in the case of the middle-frequency term ($\phi_{MF} = 0.78$). Also, a notable decrease to $\phi_{MF} = 0.63$ can further be noted, when the concentration of $NH_3$ to the anode decreases from 20 % to 10 % (Fig. 4). The observed behavior points to a solid-state diffusion-related middle-frequency process, which is shown to be dependent on $p_{H2}$ variations, approaching the characteristic value of the $\phi$ parameter for diffusion ($\phi = 0.5$) [24], when the partial pressure of $H_2$ decreases. A tentative modeling with the Finite Length Warburg (FLW) element was further conducted. In SOFCs, the FLW can describe a simultaneous combination of a one-dimensional solid-state diffusion process towards the electrolyte, denoting a high-frequency straight line ($\phi = 0.5$), but also, on the low-frequency end, a transition to a semicircle ($\phi$ closer to 1). This low-frequency capacitive part can be associated with a constant activity of the mobile species at the surface of the electrode grains [24]. In the current work, the FLW could, thus, be used to replace the $R_{MF}||CPE_{MF}$ (diffusion) and the $R_{LF}||CPE_{LF}$ (reaction) terms. Nevertheless, any tentative fitting yielded less accurate results, and its use was discarded to adjust to the present case.

Subsequently, the current–potential (*I-V*) characteristics of the stack were evaluated – Fig. 5. The dilution of the fuel gas has a considerable effect on the oxidation potential at the anode electrode, which makes the anode potential increase, reducing the potential difference – the nitrogen used for the diluting the ammonia contains trace amounts of oxygen and, as ammonia concentration decreases, the oxygen to ammonia ratio increases, which makes the potential difference of the cell to decrease. Generally, open-circuit voltage (OCP) is determined by the atmospheres of the cathode and anode, particularly in SOFC with YSZ electrolyte, in which the electronic conduction is much smaller than its ionic conduction. Considering the anionic conduction of the electrolyte, the OCP is expressed as an implicit function of the electrolyte's characteristic oxygen pressure. The partial pressure of oxygen directly influences the chemical potential of oxygen, which in turn affects the electromotive force (EMF) of the stack. The electrolyte is assumed to be a pure oxygen ion conductor, without electronic conduction, indicating zero flux of $O^{2-}$ under OCV conditions. Following equations regarding the electrochemical potentials $O^{2-}$ and $e^-$ and $O_2$, the Nernst equation can be written as [38]:

$$E_N = \frac{\widetilde{\mu_{e^-}}(c) - \widetilde{\mu_{e^-}}(a)}{-F} = \frac{\mu_{O_2}(g/c) - \mu_{O_2}(g/a)}{4F} = \frac{RT}{4F} \ln \frac{p_c}{p_a} \tag{20}$$

where 'c', 'a', and 'g' denotes cathode, anode, and electrode internal pores, respectively. Following, Equation (21) was considered to express

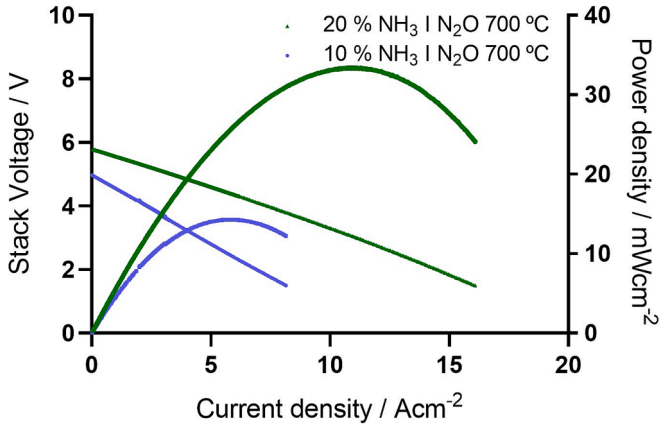


**Fig. 5.** *I-V* characteristic curves at 700 °C, feeding the anode with different $NH_3$ stream concentrations (10 % and 20 % of $NH_3$ balanced in $N_2$) and 100 % $N_2O$ to the cathode.

OCP:

$$\Delta E_{OCP} = \Delta E_0 + \left(\frac{RT}{nF}\right)\ln\left(\frac{p_{O_2,cathode}}{p_{O_2,\,anode}}\right) \quad (21)$$

where $\Delta E_{OCP}$ is the *Nernst* potential, $\Delta E_0$ is the ideal cell potential under standard-state conditions, and $p_{O_2,cathode}$ and $p_{O_2,\,anode}$ are the oxygen partial pressures of the cathode and the anode, respectively. In addition, $R$, $F$, $T$, and $n$ are the universal gas constant (8.134 $m^3$ Pa $K^{-1}$ $mol^{-1}$), the Faraday constant (96 485 C $mol^{-1}$), the sensor temperature (K), and the number of moles of electrons transferred (4 mol), respectively.

Using partial pressures simplifies the calculations, as it avoids the need to consider other species or complex reaction mechanisms. This simplification is particularly useful in SOFCs because oxygen ion conduction is a key part of the cell's operation, and the partial pressures of oxygen at the electrodes are readily measurable and controllable.

Actually, it was observed that the oxygen partial pressure ($p_{O_2}$) in the anode side increased from 4.82 x $10^{-20}$ atm to 6.17 x $10^{-19}$ atm when the fuel concentration was decreased from 20 % of $NH_3$ balanced in $N_2$ to 10 % of $NH_3$; consequently, the open circuit potential difference decreased [39]. It should be emphasized that the changes in $p_{O_2}$ are transient, returning to the initial value as soon as the feed concentration of $NH_3$ returns to the initial concentration of 20 %.

As the reduction potential increases with the $NH_3$ dilution, the nickel at the anode electrode may onset to oxidize. However, the predominance diagram obtained for the Ni–O–H system at 700°C, depicted in Fig. 6, indicates clearly that the thermodynamic limit for Ni oxidation to NiO is around $p_{O_2} \leq 10^{-16}$ atm, which lies above the values recorded in this work for diluted ammonia (feed concentration of 10 %). However, the anodic reaction produces $H_2O$ as a byproduct, which can cause the Ni grains to oxidize to NiO, resulting in a volumetric expansion of *ca*. 30 % [40]. This behavior may, thus, explain the decreased OCP value with the $NH_3$ dilution.

Meanwhile, the effect of fuel dilution is further noticed in changes in the stack performance (Fig. 5), showing a decrease in the maximum power output from 33 mW $cm^{-2}$ to 14 mW $cm^{-2}$ when reducing the $NH_3$ concentration from 20 % to 10 %. This may suggest a decrease in the rate of the electrochemical reactions, dependent on the fuel concentration. The fuel utilization at 0.7 V – typical operating potential difference – was determined following Eq. (19):

$$U_f = \frac{J \times A \times n_{cells}}{F \times n \times m_{fuel}} \quad (22)$$

Where $J$ is the current density, $A$ is the cell area, $n_{cells}$, $F$ is the Faraday constant and $m_{fuel}$ is the fuel molar flow. Values of fuel utilization for the study cases at 700°C with 20 and 10 % of ammonia in the anode side were found to be 17.0 % and 10.1 %, respectively. This point is in accordance with the Butler-Volmer equations, where the dependency on the concentration of the oxidized species directly reduces the exchange current density, affecting the kinetics of the electrochemical reactions. The results show, in agreement with Farr and Vayenas [18], that the more diluted the fuel is, the lower the power output comes. Moreover, the exchange current density depends critically on the nature of the electrode, where the formation of passivating oxides can hinder the performance. In this regard, it is observed an increase in the $R_{ohm}$ and $R_p$ terms as the anode fuel concentration decreases, corroborating the formation of NiO species at the anode and the consequent lower catalytic activity.

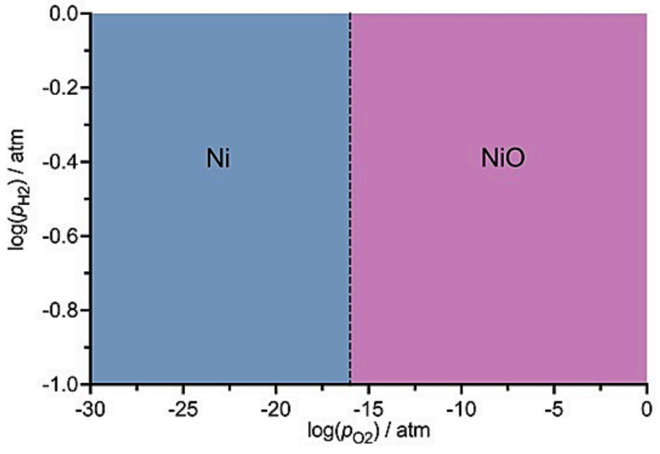


**Fig. 6.** Predominance diagram obtained at 700 °C for the Ni–O–H system. Thermodynamic calculations were made using the HSC Chemistry software [41].

### 3.3. The effect of the temperature on the electrochemical properties of the stack

The SOFC was studied under different operating temperatures, to further understand the electrochemical processes occurring in the SOFC stack. The operating temperature was varied between 600°C and 800°C; the feed conditions were kept constant with the anode fed with 20 % of $NH_3$ balanced in $N_2$ at 1200 mL $min^{-1}$, and the cathode fed with 100 % of $N_2O$ at 1680 mL $min^{-1}$. Fig. 7 shows the Nyquist plots obtained at different temperatures, under OCP conditions; Fig. 7 a) represents the equivalent circuit model used to fit the Nyquist plot presented in Fig. 7 d) and e) obtained at 700 and 600°C, respectively. Fig. 7 b) represents the equivalent circuit model used to fit the Nyquist plot data obtained at 800°C.

As the operating temperature of the SOFC stack increased, the conductivity of the electrolyte and the kinetics of the electrode's reactions increased, resulting in lower ohmic and polarization resistances, respectively.

From the DFRT shown in Fig. 7f) to h), it can be seen that the magnitude of all the individual polarization processes decreases when the temperature increases, highlighting their thermally activated nature. Furthermore, it is observed a significant shift of time constants to lower values as the temperature increases, suggesting faster reaction/diffusion in such conditions. A remarkable behavior can be observed at 800°C, when an additional peak emerged at a high time constant of 9.61 x $10^{-1}$ s – Fig. 7c), Table 3.

This peak was tentatively attributed to gas conversion/gas diffusion limitations either in the fuel electrode or in the oxidant electrode, which is relevant only at high temperatures [33,36,42,43]. In the Nyquist plot, this contribution is usually seen as an isolated and well-defined low-frequency arc [36], aligning well with what was observed in the obtained results – Fig. 7c).

In the case of the oxidant electrode, the $N_2O$ thermal decomposition at the cathode side is thermodynamically spontaneous in the whole temperature range – Fig. 8.

$$2N_2O\,(g) \rightarrow 2N_2\,(g) + O_2\,(g) \quad (23)$$

Hence, gas conversion limitations are not expected at the cathode side. Similarly, the ammonia dissociation reaction in the fuel electrode is also thermodynamically favorable above 185°C – Fig. 8:

$$2NH_3(g) \rightarrow 3H_2\,(g) + N_2(g) \quad (24)$$

The rate of ammonia thermal decomposition has an exponential dependence on the temperature, following the Arrhenius law [44]. As the temperature increases, ammonia thermal decomposition is less likely to be the limiting process. For that reason, it is very likely that $R_{gas}||CPE_{gas}$, which has an important contribution to the EIS spectrum at 800°C, may be linked to the diffusional transport of the products from this reaction, $H_2$ and $N_2$, which display a far more modest temperature dependence, $D \propto D_0 T^{1.5}$ [45]. In fact, the capacitance term of the

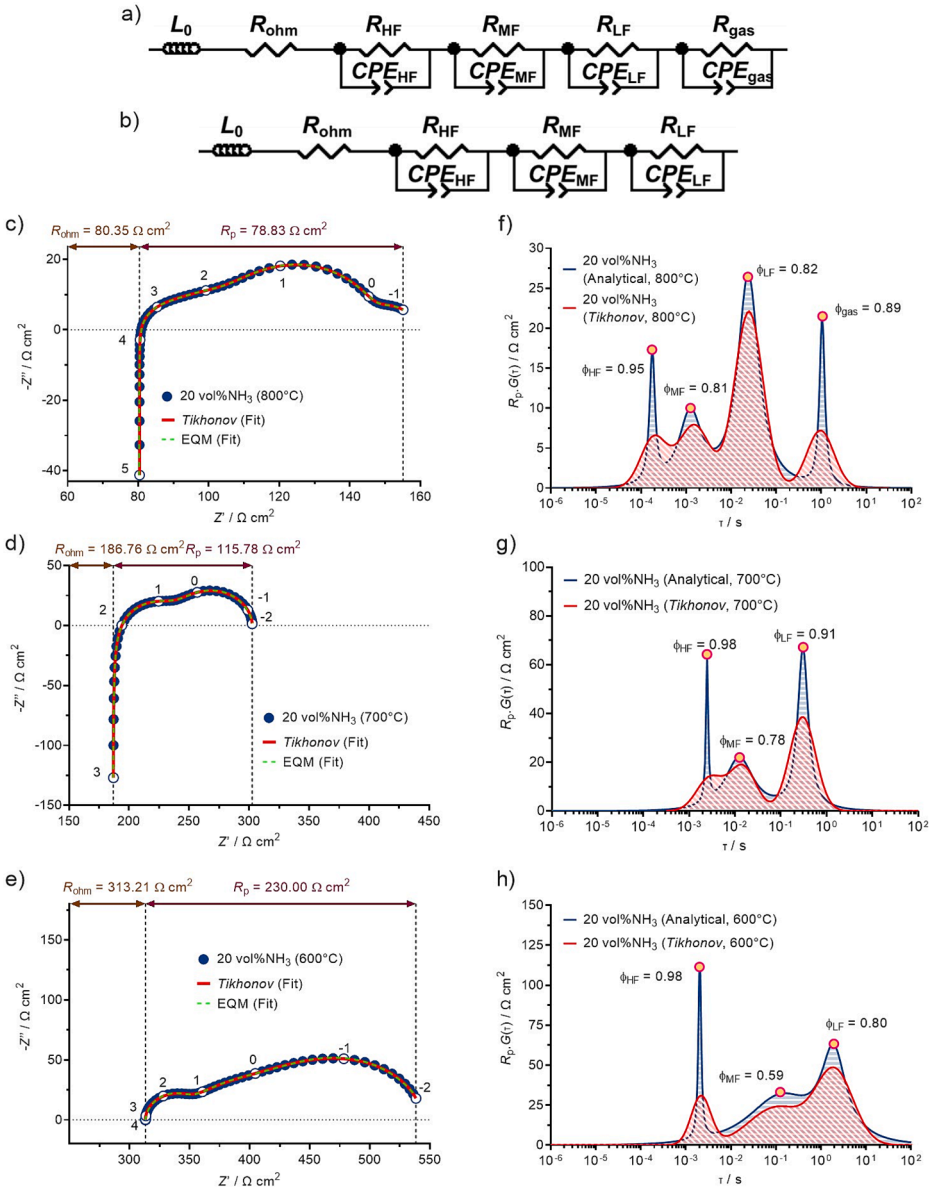


**Fig. 7.** Equivalent circuit model (ECM) used to fit the electrochemical impedance spectroscopy (EIS) experimental data under open circuit potential (OCP) conditions at a) 800 °C and b) 700 °C and 600 °C, for 20 % of $NH_3$ balanced in $N_2$ at the anode side; corresponding Nyquist plot obtained at c) 800 °C, d) 700 °C, and e) 600 °C; corresponding distribution function of relaxation times (DFRT) analyses generated by the *Tikhonov* regularization and the analytical procedure at f) 800 °C, g) 700 °C, and h) 600 °C.

semicircle becomes very high, *ca.* $10^{-2}$ F $cm^{-2}$ – Table 3 – in the typical range reported for gas-conversion/diffusion limitations [33,36,46]. When performing EIS measurements, the electrode is perturbed by the AC signal, resulting in a variation in fuel gas composition [47]. Hence, the $R_{gas}||CPE_{gas}$ process is due to a variation in the local partial pressure of reactants and products of the reaction; the AC perturbation will hardly lead to substantial changes in fuel composition as the gas flow and diffusion is much slower than the AC signal.

Another important feature noted in the DFRT plot, Fig. 7h), is related to the middle-frequency CPE exponent, $\phi_{MF}$, which was found to have the lowest value compared with the other obtained CPE exponents. This exponent was assigned to diffusion limitations in the electrodes, which are known to originate in small values and close to 0.5 [24]. Hence, the $R_{MF}||CPE_{MF}$ process is most likely related to solid-state diffusion of charge carriers/intermediate species [34,36]. Furthermore, $\phi_{MF}$ decreases from 0.81 to 0.59 when the temperature goes from 800°C to 600°C, as highlighted in Fig. 9a), which should be associated with the charge-carrier mobility decrease with the temperature [34,36]. To support these assumptions, the apparent *Warburg* capacitance [24] was determined for the $R_{MF}||CPE_{MF}$ process:

$$Y_{0,app} = \frac{(R_{MF}Y_0)^{0.5/\phi}}{R_{MF}} \quad (25)$$

Fig. 9b) presents the obtained $Y_{0,\,apparent}$ as a function of temperature for the $RC_{MF}$ element, showing a satisfactory linear dependence and underscoring the potential diffusional nature of this process.

It was further evaluated the current–potential (*I-V*) characteristics of the stack as a function of the temperature. Fig. 10 shows the results obtained for 600°C, 700°C, and 800°C, using 20 % of $NH_3$ balanced in $N_2$ feed to the anode and 100 % of $N_2O$ feed to the cathode. From Fig. 10, the variation of $\Delta E_{OCP}$ with the temperature is apparent; increasing the temperature from 700°C to 800°C, $\Delta E_{OCV}$ decreases from 5.78 V to 5.47 V – a behavior that can be predicted from the following equation [48]:

**Table 3**
Electrochemical parameters extracted from the *Tikhonov* regularization on the Electrochemical impedance spectroscopy (EIS) data obtained at 800 °C, 700 °C, and 700 °C, for 20 % of $NH_3$ balanced in $N_2$ at the anode, and 100 % of $N_2O$ at the cathode.

| DFRT peak | Parameter | 20 %$NH_3$ (800°C) | 20 %$NH_3$ (700°C) | 20 %$NH_3$ (600°C) |
|---|---|---|---|---|
| $P_1$ | $\tau_{HF}$ / s | 1.91 x $10^{-4}$ | 2.77 x $10^{-3}$ | 2.18 x $10^{-3}$ |
| | $R_{HF}$ / Ω $cm^2$ | 10.52 | 22.52 | 37.91 |
| | $C_{HF}$ / F $cm^{-2}$ | 1.82 x $10^{-5}$ | 1.23 x $10^{-4}$ | 5.75 x $10^{-5}$ |
| $P_2$ | $\tau_{MF}$ / s | 1.51 x $10^{-3}$ | 1.45 x $10^{-2}$ | 1.07 x $10^{-1}$ |
| | $R_{MF}$ / Ω $cm^2$ | 16.05 | 31.01 | 86.07 |
| | $C_{MF}$ / F $cm^{-2}$ | 9.39 x $10^{-5}$ | 4.68 x $10^{-4}$ | 1.24 x $10^{-3}$ |
| $P_3$ | $\tau_{LF}$ / s | 2.49 x $10^{-2}$ | 2.95 x $10^{-1}$ | 2.03 |
| | $R_{LF}$ / Ω $cm^2$ | 40.16 | 63.19 | 108.62 |
| | $C_{LF}$ / F $cm^{-2}$ | 6.20 x $10^{-4}$ | 4.68 x $10^{-3}$ | 1.87 x $10^{-2}$ |
| $P_4$ | $T_{gas}$ / s | 9.61 x $10^{-1}$ | – | – |
| | $R_{gas}$ / Ω $cm^2$ | 12.53 | – | – |
| | $C_{gas}$ / F $cm^{-2}$ | 7.67 x $10^{-2}$ | – | – |

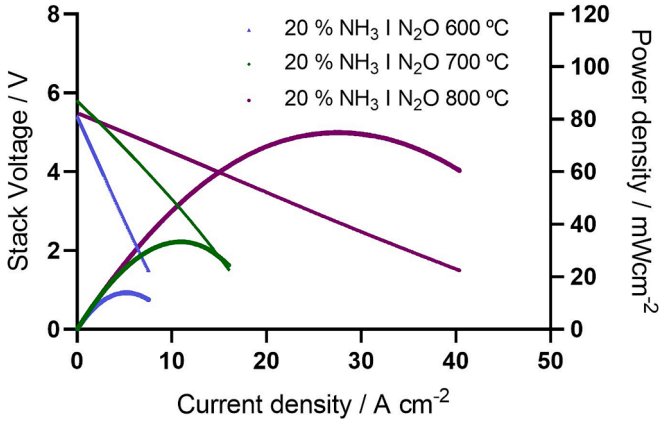


**Fig. 10.** *I-V* curves performed at 600 °C, 700 °C, and 800 °C by feeding the anode with 20 vol% of $NH_3$ and the cathode with 100 vol% of $N_2O$.

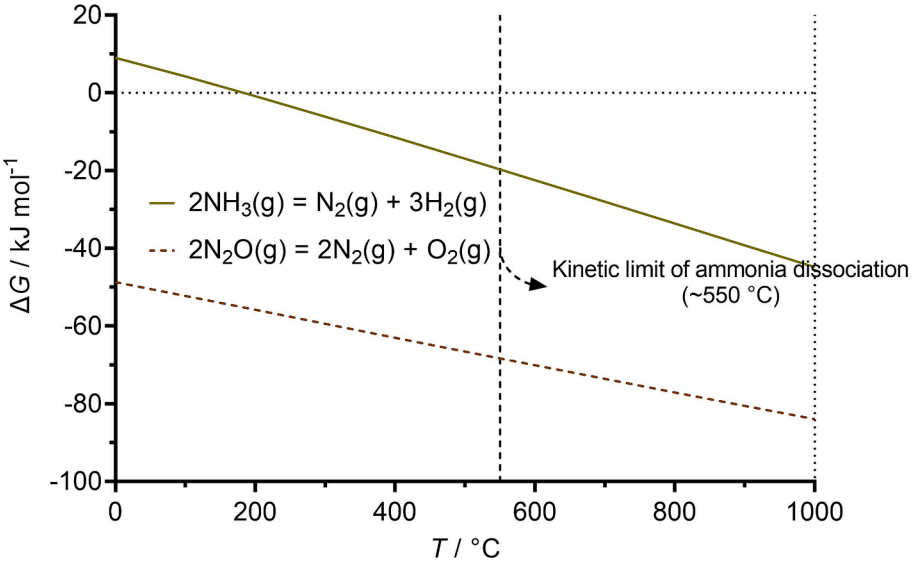


**Fig. 8.** Gibbs free energy (Δ*G* / kJ/mol) as a function of temperature (T / °C) for the ammonia and nitrous oxide decomposition reactions. Thermodynamic data collected from HSC chemistry software [41].

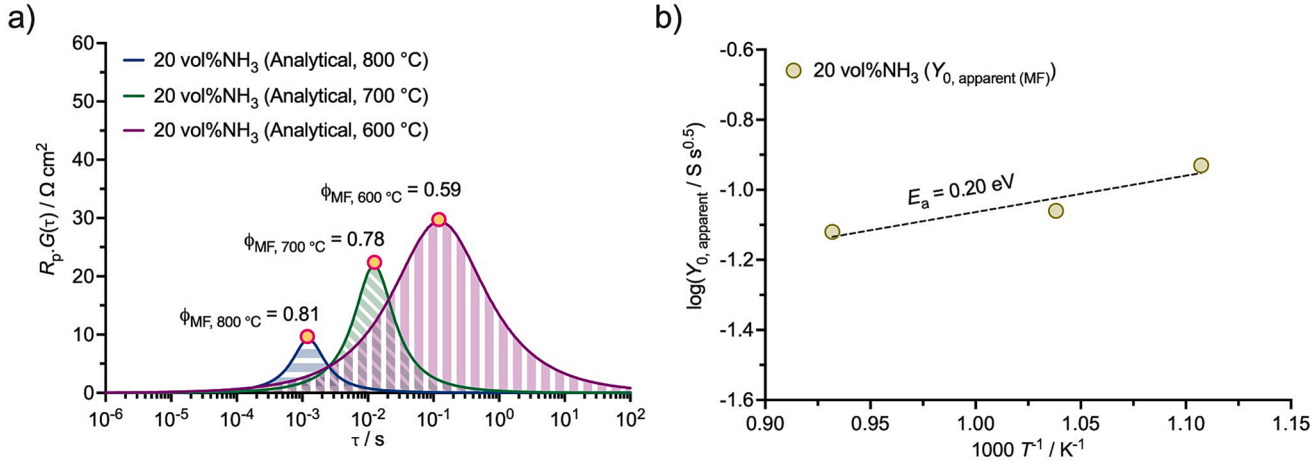


**Fig. 9.** a) the middle-frequency process of thedistribution function of relaxation times (DFRT) analyses generated by the analytical procedure in the temperature range of 600 °C to 800 °C; b) the temperature dependency of the apparent *Warburg* capacitance ($Y_{0,\ app}$), obtained with Eq (25).

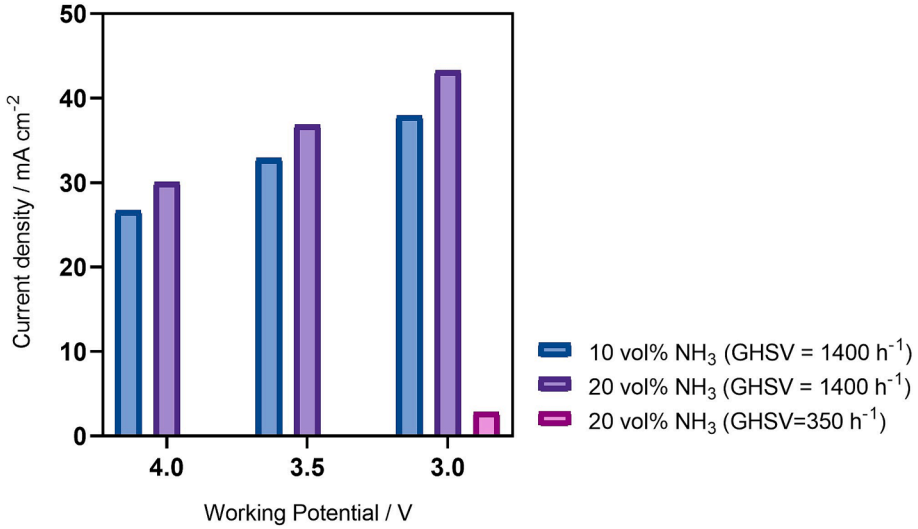


**Fig. 11.** Polarization experiments toward NO production at 700 °C for different fuel concentrations (10 vol% and 20 vol% of $NH_3$ balanced in $N_2$ at the anode and 100 vol% of $N_2O$ at the cathode): current density as a function of applied voltage (3 V, 3.5 V, and 4 V). The tests were performed using two different gas hourly space velocities (GHSV) (1400 and 350 $h^{-1}$), which was calculated gas flow rate (1200 mL $min^{-1}$ and 300 mL $min^{-1}$)by dividing the stack volume (51.52 $cm^3$).

$$\Delta E_{OCP} = \Delta E_0 + \left(\frac{\Delta S}{nF}\right)(T - T_0) \tag{26}$$

where $\Delta S$ is the reaction entropy, $T$ is the operating temperature, and $T_0$ is the reference temperature (298.15 K).

In this case, the thermodynamic potential difference of the hydrogen oxidation reaction is related to the Gibbs free energy according to the equation [49]:

$$\Delta E = -\frac{\Delta G}{nF} \tag{27}$$

and the free energy of Gibbs can be written as [49]:

$$\Delta G = \Delta H - T\Delta S \tag{28}$$

For the hydrogen oxidation reaction $\Delta H$, it is negative, meaning the reaction is exothermic and $\Delta S$ is also negative. As the temperature increases, $\Delta G$ normally decreases, and then decreases the potential difference of the reaction.

As the temperature increases, the ammonia decomposition reaction rate increases, and since the reaction is endothermic (Eq. (21)) and equilibrium limited, the reaction equilibrium conversion also shifts to higher hydrogen concentrations. The increase in hydrogen concentration makes the potential difference shift to higher values.

Fig. 10 shows that the open circuit potential difference at 600°C is 5.40 V, lower than at 700°C and 800°C. This result was tentatively attributed to hydrogen starvation because of a low ammonia decomposition reaction rate; actually, the ammonia decomposition reaction rate becomes noticeable only for > 550°C [17].

Likewise, the power output increases mostly linearly (Fig. S.1 in SI), achieving peak power densities of 14 mW $cm^{-2}$, 33 mW $cm^{-2}$, and 70 mW $cm^{-2}$, respectively, at 600°C, 700°C, and 800°C. It should be emphasized that the electrochemical oxidation rate is also a function of the current density at which the cell is operated. In fact, upon increasing the temperature and under-applied polarization, the fuel/oxidant utilization increases due to increased electrode kinetics [33]. Then, the rate of product formation ($H_2O/N_2$ at the anode and $O_2/N_2$ at the cathode) increases, resulting in a concomitant increase in the power output. Nevertheless, these assumptions need further investigation.

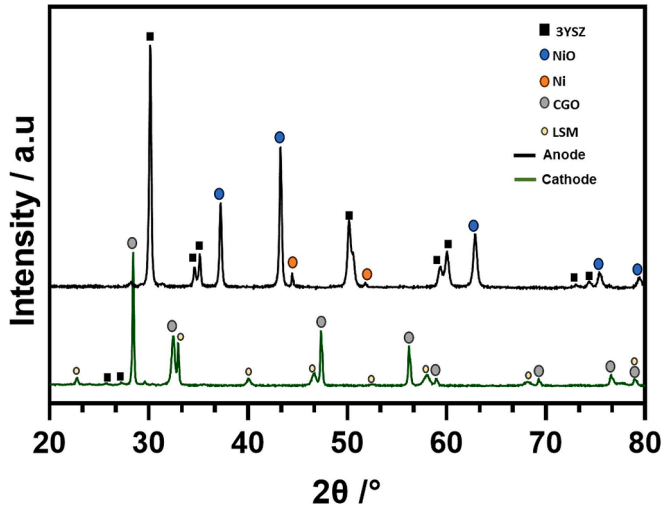


**Fig. 12.** Post-mortem X-ray diffraction (XRD) analysis of a representative membrane electrode assembly (MEA) composing the SOFC stack.

### 3.4. Electrochemical nitrogen oxide (NO) production

The previous sections focused on describing the main electrochemical processes occurring on the electrodes, particularly on the anode side; it was concluded about the importance of the fuel concentration and the operating temperature.

This section studies the production of NO (the final goal of the current work) using the SOFC stack. To produce NO, it is necessary to decrease the gas hourly space velocity (GHSV); GHSV describes the volumetric flow rate of a gas through the catalyst bed relative to the volume of the reactor or by the mass of the catalyst. This metric is calculated by dividing the volumetric feed flow rate of the gas by the volume of the reactor, in this case of the stack, or by the mass of the catalyst. Following, the anode feed flow rate was decreased from 1200 mL $min^{-1}$ to 300 mL $min^{-1,}$ and the cathode decreased from 1680 mL $min^{-1}$ to 300 mL $min^{-1}$, from the first to the second experiment. The GHSV has a significant impact on the electrocatalytic reactions; a lower GHSV allows for a longer interaction of the gaseous chemical reagents with the electrocatalyst [18,50], *i.e.*, the nitrogen radical (N*) formed at the anode interacts with the oxygen ions coming from the cathode to produce NO [18]:

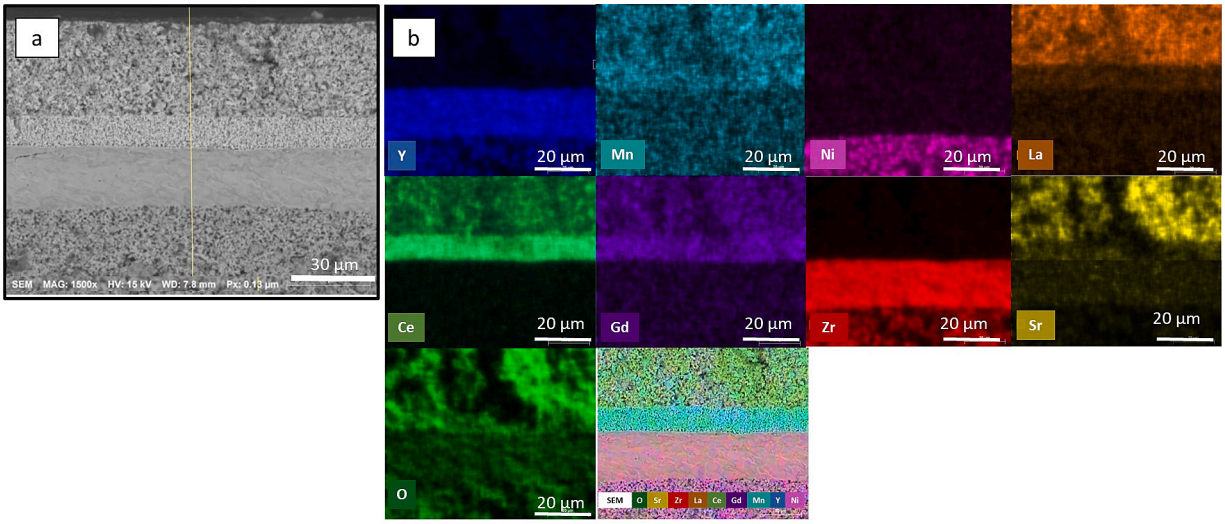


**Fig. 13.** A)Scanning electron microscopy (SEM) cross-section microstructure of a representative MEA membrane electrode assembly (MEA) composing the SOFC stack and b) its respective EDS mapping images.

$$2NH_3(g) + 5O^{2-} \rightarrow 2NO(g) + 3H_2O(g) + 10e^- \quad (29)$$

Eq. (24) is, therefore, controlled by the solid-state diffusion rate of $O^{2-}$, and then proportional to the current, according to *Faraday's* Law:

$$i = nFN_{O^{2-}} \quad (30)$$

where $i$ is the current density, F is the Faraday constant, and $N_{O^{2-}}$ is the $O^{2-}$ permeate rate. The proposed equation for the overall reaction taking place at the TPBs of the anode electrode is:

$$H_2(g) + 0.5N_2(g) + 2O_O^x(YSZ) \rightarrow H_2O(g) + NO(g) + 2V_O^{\bullet\bullet}(YSZ) + 4e^-(Ni) \quad (31)$$

This equation is similar to Eq. (15), which was proposed for the hydrogen oxidation reaction.

The stack was first tested at a fixed temperature of 700°C, fed with 20 % of $NH_3$ balanced in $N_2$ at the anode and 100 % of $N_2O$ at the cathode, at 1200 mL $min^{-1}$ and 1680 mL $min^{-1}$, respectively. The polarization experiments were performed under applied polarizations of 3 V, 3.5 V, and 4 V. The stack current density is presented in Fig. 11.

The polarization tests were initially performed for 20 min, but NO was not detected. The reason for the absence of NO might be explained by the excessive GHSV, particularly in the anodic compartment (*i.e.*, high flow of $O^{2-}$ compared with $NH_3$). Following, in the second experiment, the GHSV was lowered four times (from *ca.* 1400 $h^{-1}$ to ca. 350 $h^{-1}$), which corresponds to a decrease in the anode and cathode feed flow rates to 300 mL $min^{-1}$. The NO production at 3 V was continuously measured, showing a selectivity to NO of 20.4 % – the ratio between the obtained amount of desired product (NO) to the used amount of a key reactant ($NH_3$), Eq. (27):

$$\text{Selectivity} = \frac{[NO]}{[NH_3]} \times 100 \quad (32)$$

where [NO] and [$NH_3$] are the molar concentrations of NO and $NH_3$ in the product stream. This value is rather low when compared with the selectivity reported by Farr & Vayenas [18] of 97 %. The lower selectivity value obtained was assigned to the activity of the undesired side reaction:

$$2NH_3(g) + 3NO(g) \rightarrow \frac{5}{2}N_2(g) + 3H_2O(g) \quad (33)$$

which can be mitigated by increasing the ratio of $NH_3$ to $O^{2-}$ concentrations at the anode side. Also, Farr & Vayenas [18] used a Pt-based anode catalyst, which was [16] possibly a superior catalyst for NO production than that of Ni used in the fuel cell stack of the current work. The conversion of the pure $N_2O$ feed at the cathode reached 50.4 %, a promising value compared to the reported 30 % obtained by Li *et al* [9].

Regarding the performance of the SOFC stack, a drastic decrease in the current density can be observed as the GHSV decreases from 43.2 mA $cm^{-2}$ (GHSV = 1400 $h^{-1}$) to 2.8 mA $cm^{-2}$ (GHSV = 350 $h^{-1}$). Nonetheless, the stack energy efficiency – Eq. (29) – based on the lower heating value of ammonia fuel, was *ca.* 87.76 %, and the fuel conversion was ca. 100 %.

$$\text{Stack Energy Efficiency} = \frac{P_{el}}{H_{LHV} \times m_{fuel}} \quad (34)$$

where $P_{el}$ is the electrical power produced by the stack, $H_{LHV}$ is the lower heating value of $NH_3$, and $m_{fuel}$ is the fuel molar flow rate.

Overall, despite the relatively lower values of NO selectivity, the power output values are encouraging, being almost 14 times higher than those reported by Farr & Vayenas [18] (*i.e.*, 8.4 mW $cm^{-2}$ *vs.* 0.61 mW $cm^{-2}$). Regarding selectivity, it is very important to highlight the nature of the catalyst materials. The employed stack was designed as a SOFC; the anode was not tailored to oxidize ammonia to NO. As a future work, a SOFC stack with an optimized anode for this reaction should be fabricated. This anode may contain cobalt since this metal catalyst was identified as rather active and selective for the pertinent reaction [51].

### 3.5. Post-mortem characterization of the stack

The *post-mortem* MEAs that compose the SOFC stack were investigated. The electrodes' surfaces were initially analyzed by X-ray diffraction (XRD). Fig. 12 shows the patterns of an anode and a cathode of a representative MEA. In both patterns, there is no evidence of any secondary phases since all peaks were indexed to the expected phases. In this regard, concerning the cathode pattern, both LSM and CGO20 phases were detected, corresponding to the cathode and buffer layers, respectively. In contrast, the anode pattern shows the presence of 8YSZ, NiO, and Ni; the presence of NiO is related to the nickel oxidation during the adopted cool-down procedure.

The microstructure of a representative MEA was also analyzed by scanning electron microscopy (SEM), to assess any morphological aging of the electrodes. Fig. 13a) shows the corresponding cross-section microstructure, which reveals a crack-free and well-densified electrolyte, in agreement with the high OCP observed during the experiments. In addition, the energy dispersive spectroscopy (EDS) images, presented

in Fig. 13b), show no migration of the metal elements across adjacent layers, reinforcing the results already obtained by XRD, which shows no secondary phases in each layer (Fig. 12).

## 4. Conclusions

This work studies the feasibility of using a SOFC system for the abatement of $N_2O$ emissions, a rather harmful and strong greenhouse effect gas, using diluted ammonia fed to the anode as a fuel. The use of ammonia instead of $H_2$ as a fuel proved to be very attractive not only because it is nonflammable, easy to hand, and usually available at chemical plants, but also because it enables the simultaneous production of NO, a valuable precursor in nitric acid production. It was obtained a high energy efficiency of 88 %, a modest selectivity to NO of 20 %, and a conversion of 50 % of the pure $N_2O$ feed to nitrogen (within the precision of the analyzer, <1–10 ppm).

Electrochemical impedance spectroscopy was successfully employed to analyze the main electrochemical processes occurring in the electrodes. The use of the Distribution Function of Relaxation Times (DFRT) was crucial to analyze the impedance data without prior knowledge of the nature of the reactions, allowing the differentiation of three main polarization processes based on their characteristic relaxation times. The use of an equivalent circuit model to analyze the experimental results obtained at different temperatures and fuel concentrations allowed to identify important electrochemical processes occurring in the SOFC stack. The discussion focused on the anode reactions, where it was found a limiting $H_2$ adsorption/desorption process occurring on the surface of the anode electrocatalyst – P3, and a charge-transfer process limitation – P1, which possibly takes place in the triple phase boundaries (TPBs). An additional diffusion process probably related to the diffusion of charge carriers/intermediate species to the TPBs was also identified – P2.

The electrochemical abatement of $N_2O$ and the electrochemical oxidation of ammonia allow NO production when operating under low gas hourly space velocity at the anode. The simultaneous abatement of $N_2O$ and the production of NO, a critical feedstock to the nitric acid industry, in a single device is an elegant example of the implementation of a process intensification strategy. This work reports very encouraging results, which justify the continuation of the research following this pathway.

## CRediT authorship contribution statement

**Celina Fernandes:** Writing – original draft, Methodology, Investigation, Formal analysis, Conceptualization. **Laura I.V. Holz:** Writing – review & editing, Methodology, Formal analysis. **Francisco J.A. Loureiro:** Writing – review & editing, Methodology, Funding acquisition, Formal analysis. **Miguel Duarte:** Writing – review & editing, Investigation. **Duncan P. Fagg:** . **Adélio Mendes:** Writing – review & editing, Supervision, Resources, Funding acquisition, Formal analysis.

## Declaration of competing interest

The authors declare that they have no known competing financial interests or personal relationships that could have appeared to influence the work reported in this paper.

## Acknowledgments

This work was supported by national funds through FCT/MCTES (PIDDAC): LEPABE, UIDB/00511/2020 (DOI: 10.54499/UIDB/00511/2020) and UIDP/00511/2020 (DOI: 10.54499/UIDP/00511/2020) and ALiCE, LA/P/0045/2020 (DOI:10.54499/LA/P/0045/2020); Agenda "H2Driven Green Agenda", nr. C644923817-00000037, investment project nr. 50, financed by the Recovery and Resilience Plan (PRR) and by European Union - NextGeneration EU. This work was also financially supported by Agência Nacional de Inovação – Project number POCI-01-0247-FEDER-039926. The authors also acknowledge the grants/projects with references https://doi.org/10.54499/2020.02797.CEECIND/CP1589/CT0030, https://doi.org/10.54499/PTDC/CTM-CTM/2156/2020, https://doi.org/10.54499/PTDC/QUI-ELT/3681/2020, https://doi.org/10.54499/2022.09319.PTDC, https://doi.org/10.54499/2022.02498.PTDC, https://doi.org/10.54499/UIDB/00481/2020, and https://doi.org/10.54499/UIDP/00481/2020 from Fundação para a Ciência e a Tecnologia (FCT), and CENTRO-01-0145-FEDER-022083 from Centro Portugal Regional Operational Programme (Centro2020), under the PORTUGAL 2020 Partnership Agreement, through the European Regional Development Fund (ERDF). Celina Fernandes wants to acknowledge to FCT for the PhD grant 2021. 07014.BD and Laura Holz acknowledge to FCT for the CEEC grant 2023.05868.CEECIND.

## Appendix A. Supplementary data

Supplementary data to this article can be found online at https://doi.org/10.1016/j.cej.2024.157921.

## Data availability

Data will be made available on request.

## References

[1] L. Alves, L.I.V. Holz, C. Fernandes, P. Ribeirinha, D. Mendes, D.P. Fagg, A. Mendes, A comprehensive review of NOx and N2O mitigation from industrial streams, Renew. Sustain. Energy Rev. 155 (2022) 111916, https://doi.org/10.1016/j.rser.2021.111916.
[2] X.“, ”K. W.T. “E. J.D. ”Lan, Trends in globally-averaged CH4, N2O, and SF6 determined from NOAA Global Monitoring Laboratory measurements, (2024).
[3] J. Pérez-Ramírez, F. Kapteijn, K. Schöffel, J.A. Moulijn, Formation and control of N2O in nitric acid production, Appl Catal B 44 (2003) 117–151, https://doi.org/10.1016/S0926-3373(03)00026-2.
[4] J. Pérez-Ramírez, B. Vigeland, Perovskite Membranes in Ammonia Oxidation: Towards Process Intensification in Nitric Acid Manufacture, Angew. Chem. Int. Ed. 44 (2005) 1112–1115, https://doi.org/10.1002/anie.200462024.
[5] C.A. Grande, K.A. Andreassen, J.H. Cavka, D. Waller, O.A. Lorentsen, H. Øien, H. J. Zander, S. Poulston, S. García, D. Modeshia, Process Intensification in Nitric Acid Plants by Catalytic Oxidation of Nitric Oxide, Ind. Eng. Chem. Res. 57 (2018) 10180–10186, https://doi.org/10.1021/acs.iecr.8b01483.
[6] statista, Production of ammonia worldwide from 2010 to 2023, (2024). https://www.statista.com/statistics/1266378/global-ammonia-production/#:~:text=In%202023%2C%20the%20global%20production%20of%20ammonia%20was,of%20ammonia%20with%20approximately%2064.6%20million%20metric%20tons. (accessed September 27, 2024).
[7] K. Sundmacher, L.K. Rihko-Struckmann, V. Galvita, Solid electrolyte membrane reactors: Status and trends, Catal. Today 104 (2005) 185–199, https://doi.org/10.1016/j.cattod.2005.03.074.
[8] V. Kyriakou, I. Garagounis, E. Vasileiou, A. Vourros, M. Stoukides, Progress in the Electrochemical Synthesis of Ammonia, Catal. Today 286 (2017) 2–13, https://doi.org/10.1016/j.cattod.2016.06.014.
[9] T. Li, M.F. Rabuni, L. Kleiminger, B. Wang, G.H. Kelsall, U.W. Hartley, K. Li, A highly-robust solid oxide fuel cell (SOFC): simultaneous greenhouse gas treatment and clean energy generation, Energ. Environ. Sci. 9 (2016) 3682–3686, https://doi.org/10.1039/C6EE02562E.
[10] A.I. Osman, N. Mehta, A.M. Elgarahy, M. Hefny, A. Al-Hinai, A.H. Al-Muhtaseb, D. W. Rooney, Hydrogen production, storage, utilisation and environmental impacts: a review, Environ. Chem. Lett. 20 (2022) 153–188, https://doi.org/10.1007/s10311-021-01322-8.
[11] C. Zamfirescu, I. Dincer, Ammonia as a green fuel and hydrogen source for vehicular applications, Fuel Process. Technol. 90 (2009) 729–737, https://doi.org/10.1016/j.fuproc.2009.02.004.
[12] G. Cinti, G. Discepoli, E. Sisani, U. Desideri, SOFC operating with ammonia: Stack test and system analysis, Int. J. Hydrogen Energy 41 (2016) 13583–13590, https://doi.org/10.1016/j.ijhydene.2016.06.070.
[13] O. Siddiqui, I. Dincer, A review and comparative assessment of direct ammonia fuel cells, Therm. Sci. Eng. Prog. 5 (2018) 568–578, https://doi.org/10.1016/j.tsep.2018.02.011.
[14] G. Cinti, V. Liso, S.S. Araya, Design improvements for ammonia-fed SOFC systems through power rating, cascade design and fuel recirculation, Int. J. Hydrogen Energy 48 (2023) 15269–15279, https://doi.org/10.1016/j.ijhydene.2023.01.008.
[15] L. Barelli, G. Bidini, G. Cinti, Operation of a Solid Oxide Fuel Cell Based Power System with Ammonia as a Fuel: Experimental Test and System Design, Energies (basel) 13 (2020) 6173, https://doi.org/10.3390/en13236173.
[16] G. Cinti, U. Desideri, D. Penchini, G. Discepoli, Experimental Analysis of SOFC Fuelled by Ammonia, Fuel Cells 14 (2014) 221–230, https://doi.org/10.1002/fuce.201300276.

[17] M. Duarte, L.I.V. Holz, C. Fernandes, P. Ribeirinha, D.P. Fagg, A. Mendes, Modelling ammonia and nitrous oxide decomposition reactions in solid oxide fuel cells for combined energy generation and treatment of flue gas streams, Appl. Energy 368 (2024) 123465, https://doi.org/10.1016/j.apenergy.2024.123465.
[18] R.D. Farr, C.G. Vayenas, Ammonia High Temperature Solid Electrolyte Fuel Cell, J. Electrochem. Soc. 127 (1980) 1478–1483, https://doi.org/10.1149/1.2129934.
[19] C.T.V.C.G. Sigal, Ammonia Oxidation to Nitric Oxide in a Solid Electrolyte Fuel Cell, Solid State Ion. 5 (1981) 567–570.
[20] SOFCMAN, Powders-Cathodes-LSM, (2023). http://61.153.149.30/lsm.asp (accessed February 7, 2024).
[21] SOFCMAN, Powders-Anodes-NiO, (2023). http://61.153.149.30/nio.asp (accessed February 7, 2024).
[22] SOFCMAN, Powders-Electrolytes-YSZ, (2023). http://61.153.149.30/ysz.asp (accessed February 7, 2024).
[23] SOFCMAN, Powders-Electrolytes-GDC, (2023). http://61.153.149.30/cgo.asp (accessed February 7, 2024).
[24] B.A. Boukamp, A. Rolle, Analysis and Application of Distribution of Relaxation Times in Solid State Ionics, Solid State Ion. 302 (2017) 12–18, https://doi.org/10.1016/j.ssi.2016.10.009.
[25] B.A. Boukamp, A. Rolle, Use of a distribution function of relaxation times (DFRT) in impedance analysis of SOFC electrodes, Solid State Ion. 314 (2018) 103–111, https://doi.org/10.1016/j.ssi.2017.11.021.
[26] F. Ciucci, Modeling electrochemical impedance spectroscopy, Curr. Opin. Electrochem. 13 (2019) 132–139, https://doi.org/10.1016/j.coelec.2018.12.003.
[27] T.H. Wan, M. Saccoccio, C. Chen, F. Ciucci, Influence of the Discretization Methods on the Distribution of Relaxation Times Deconvolution: Implementing Radial Basis Functions with DRTtools, Electrochim. Acta 184 (2015) 483–499, https://doi.org/10.1016/j.electacta.2015.09.097.
[28] B.M.G. Melo, F.J.A. Loureiro, D.P. Fagg, L.C. Costa, M.P.F. Graça, DFRTtoEIS: An easy approach to verify the consistency of a DFRT generated from an impedance spectrum, Electrochim. Acta 366 (2021) 137429, https://doi.org/10.1016/j.electacta.2020.137429.
[29] F.J.A. Loureiro, D. Ramasamy, V.C.D. Graça, L.I.V. Holz, S.M. Mikhalev, D.P. Fagg, Analysis of $La_4Ni_3O_{10\pm\delta}$-$BaCe_{0.9}Y_{0.1}O_{3-\delta}$ Composite Cathodes for Proton Ceramic Fuel Cells, Appl. Sci. 11 (2021) 3407, https://doi.org/10.3390/app11083407.
[30] O.A. Ojelade, S.F. Zaman, Ammonia decomposition for hydrogen production: a thermodynamic study, Chem. Pap. 75 (2021) 57–65, https://doi.org/10.1007/s11696-020-01278-z.
[31] L. Bi, E. Fabbri, Z. Sun, E. Traversa, BaZr0.8Y0.2O3−δ-NiO Composite Anodic Powders for Proton-Conducting SOFCs Prepared by a Combustion Method, J. Electrochem. Soc. 158 (2011) B797, https://doi.org/10.1149/1.3591040/XML.
[32] N. Nasani, D. Ramasamy, A.D. Brandão, A.A. Yaremchenko, D.P. Fagg, The impact of porosity, pH2 and pH2O on the polarisation resistance of Ni–BaZr0.85Y0.15O3−δ cermet anodes for Protonic Ceramic Fuel Cells (PCFCs), Int. J. Hydrogen Energy 39 (2014) 21231–21241, https://doi.org/10.1016/J.IJHYDENE.2014.10.093.
[33] L.I.V. Holz, F.J.A. Loureiro, V.C.D. Graça, S.M. Mikhalev, D. Mendes, A. Mendes, D. P. Fagg, Vanadium (oxy)nitride as a new category of anode for direct ammonia solid oxide fuel cells cells, Renew. Energy 201 (2022) 124–130, https://doi.org/10.1016/j.renene.2022.10.098.
[34] E.B.G.A. Fulgêncio, F.J.A. Loureiro, K.P.V. Melo, R.M. Silva, D.P. Fagg, L.F. A. Campos, D.A. Macedo, Boosting the oxygen reduction reaction of the misfit $[Ca_2CoO_{3-\delta}]_q[CoO_2]$ (C349) by the addition of praseodymium oxide, J. Alloy. Compd. 788 (2019) 148–154, https://doi.org/10.1016/j.jallcom.2019.02.209.
[35] A.J.M. Araújo, V.C.D. Graça, R.A. Raimundo, A.C.L. Filho, D.A. Macedo, F.J. A. Loureiro, A new layered barium cobaltite electrode for protonic ceramic cells, J. Mater. Chem. A Mater. (2024), https://doi.org/10.1039/D3TA06438G.
[36] S. Primdahl, M. Mogensen, Gas Diffusion Impedance in Characterization of Solid Oxide Fuel Cell Anodes, J. Electrochem. Soc. 146 (1999) 2827–2833, https://doi.org/10.1149/1.1392015.
[37] W. Choi, H.-C. Shin, J.M. Kim, J.-Y. Choi, W.-S. Yoon, Modeling and Applications of Electrochemical Impedance Spectroscopy (EIS) for Lithium-ion Batteries, J. Electrochem. Sci. Technol. 11 (2020) 1–13, https://doi.org/10.33961/jecst.2019.00528.
[38] Y. Zhang, Y. Chen, M. Yan, An open circuit voltage equation enabling separation of cathode and anode polarization resistances of ceria electrolyte based solid oxide fuel cells, J. Power Sources 357 (2017) 173–178, https://doi.org/10.1016/j.jpowsour.2017.04.096.
[39] N. Mahato, A. Banerjee, A. Gupta, S. Omar, K. Balani, Progress in material selection for solid oxide fuel cell technology: A review, Prog. Mater Sci. 72 (2015) 141–337, https://doi.org/10.1016/j.pmatsci.2015.01.001.
[40] S. Dierickx, A. Weber, E. Ivers-Tiffée, How the distribution of relaxation times enhances complex equivalent circuit models for fuel cells, Electrochim. Acta 355 (2020) 136764, https://doi.org/10.1016/j.electacta.2020.136764.
[41] A. Roine, HSC Chemistry® [Software], (2021). https://www.mogroup.com/hsc.
[42] A. Mohammed Hussain, J.V.T. Høgh, T. Jacobsen, N. Bonanos, Nickel-ceria infiltrated Nb-doped SrTiO3 for low temperature SOFC anodes and analysis on gas diffusion impedance, Int. J. Hydrogen Energy 37 (2012) 4309–4318, https://doi.org/10.1016/j.ijhydene.2011.11.087.
[43] T. Jacobsen, P.V. Hendriksen, S. Koch, Diffusion and conversion impedance in solid oxide fuel cells, Electrochim. Acta 53 (2008) 7500–7508, https://doi.org/10.1016/j.electacta.2008.02.019.
[44] H.E. Avery, Dependence of Rate on Temperature, in: Basic Reaction Kinetics and Mechanisms, Macmillan Education UK, London, 1974: pp. 47–58. https://doi.org/10.1007/978-1-349-15520-0_4.
[45] P.P. de J. "Keeler, J. "Atkins, Physical Chemistry, 12th ed., Oxford University Press, 2022.
[46] D.A. Osinkin, B.L. Kuzin, N.M. Bogdanovich, Gas diffusion hindrances on Ni cermet anode in contact with Zr0.84Y0.16O1.92 solid electrolyte, Russ. J. Electrochem. 45 (2009) 483–489, https://doi.org/10.1134/S102319350904020X.
[47] S. Primdahl, M. Mogensen, Gas Conversion Impedance: A Test Geometry Effect in Characterization of Solid Oxide Fuel Cell Anodes, J. Electrochem. Soc. 145 (1998) 2431–2438, https://doi.org/10.1149/1.1838654.
[48] G. Meng, C. Jiang, J. Ma, Q. Ma, X. Liu, Comparative study on the performance of a SDC-based SOFC fueled by ammonia and hydrogen, J. Power Sources 173 (2007) 189–193, https://doi.org/10.1016/j.jpowsour.2007.05.002.
[49] R.C.S.-W.C.W.P.F.B. O'Hayre, Fuel Cell Fundamentals , John Wiley & Sons, Inc., New Jersey, 2006.
[50] M.D. Johnson, S.A. May, J.M.C. Groh, L.P. Webster, V. Shankarraman, R. D. Spencer, C.V. Luciani, C.S. Polster, T. Braden, Understanding Residence Time, Residence Time Distribution, and Impact of Surge Vessels, In (2020) 51–85, https://doi.org/10.1007/978-3-030-41524-2_3.
[51] N.M. Sammes, B.C.H. Steele, The Catalytic Oxidation of Ammonia in a Ceramic Electrochemical Reactor, Using Metal Oxide Electrodes, J Catal 145 (1994) 187–193, https://doi.org/10.1006/jcat.1994.1022.